Article

Current Harmonics Suppression of Six-Phase Permanent-Magnet Synchronous Motor Drives Using Back-Electromotive Force Harmonics Compensation

Po-Sheng Huang [1], Cheng-Ting Tsai [1], Jonq-Chin Hwang [1,*], Cheng-Tsung Lin [2] and Yu-Ting Lin [2]

1 Department of Electrical Engineering, National Taiwan University of Science and Technology, Taipei City 106, Taiwan
2 Chroma ATE Inc., Taoyuan City 333, Taiwan
* Correspondence: jchwang@mail.ntust.edu.tw

Abstract: This paper investigates a back-electromotive force (EMF) harmonic compensation strategy for six-phase permanent-magnet synchronous motors (PMSMs) to reduce current harmonics and improve system performance. Ideally, the back-EMF waveform should be perfectly sinusoidal. However, manufacturing imperfections such as suboptimal magnetic circuit design, uneven winding distribution, and mechanical eccentricity introduce low-order spatial harmonics, particularly the 5th, 7th, 11th, and 13th orders, which distort the back-EMF, increase current harmonics, complicate control, and reduce efficiency. To address these issues, this study proposes a compensation strategy utilizing common-mode and differential-mode current control. By injecting the 6th and 12th harmonics into the decoupled voltage commands along the d-axis and q-axis, the strategy significantly reduces current harmonic distortion. Experimental validation was conducted using a TMS320F28386D microcontroller, which controlled dual inverters via PWM signals and processed real-time current feedback. Rotor position feedback was provided by a resolver to ensure precise and responsive motor control. At a rotational speed of 900 rpm, with a peak phase current I_m of 200 A and an IGBT switching frequency of 10 kHz, the phase-*a* current total harmonic distortion (THD) was reduced from 11.86% (without compensation) to 6.83% (with compensation). This study focused on mitigating harmonics below the 14th order. The experimental results demonstrate that the proposed back-EMF harmonic compensation strategy effectively minimizes current THD, highlighting its potential for improving the performance and efficiency of multi-phase motor systems.

Keywords: current harmonics; six-phase PMSM; common mode and differential mode; back-EMF harmonic compensation

1. Introduction

In modern applications, both three-phase and six-phase PMSMs are widely utilized across industrial and consumer sectors [1–9]. In recent years, the control of six-phase PMSMs has garnered significant attention, with numerous studies demonstrating the advantages [10–12]. Therefore, these benefits will not be further elaborated on in this paper. The fundamental specifications of the six-phase PMSM under test can be found in Appendix A Table A1. The motor is controlled using common-mode and differential-mode current control strategies [13]. Specifically, the control involves summing and subtracting the dq-axes currents of the two three-phase sets within a six-phase system, following the principles of field-oriented control (FOC) [14,15].

Initially, this method failed to achieve satisfactory control performance, with the total harmonic distortion (THD) of the six-phase currents exceeding 10%. Excessive current harmonic distortion leads to torque ripple, which can affect the motor's smooth operation and potentially shorten the lifespan of mechanical components. One of the primary causes of current harmonics is the harmonics of back-EMF, which can directly induce and amplify

current harmonics by affecting the motor's electromagnetic interactions, nonlinear load characteristics, the dynamic response of the control system, and internal electromagnetic force variations, also resulting in torque ripple [16–18]. Hence, it is clear that reducing back-EMF harmonics can significantly enhance motor performance. By applying back-EMF compensation techniques, as described in [19], overall operating performance can be effectively improved. While that approach does not go into detail on phases of harmonics during back-EMF harmonic compensation, this work takes the harmonic phases into account to offer a more complete perspective on optimizing compensation accuracy.

This paper analyzes the harmonics of the back-EMF, focusing not only on the magnitudes of the 5th, 7th, 11th, and 13th harmonics but also the phases [20] to reconstruct the original back-EMF waveform. The 5th, 7th, 11th, and 13th harmonics of phase back-EMF are derived into 6th and 12th harmonics of the d-axis and q-axis back-EMF through Clarke and Park transformations [21,22], simplifying the mathematical model of back-EMF compensation strategy.

Related studies have explored optimization strategies to further enhance system performance and stability. For instance, inertial control strategies and optimization of control parameters have been shown to improve system stability and dynamic response under varying conditions [23–27]. Incorporating insights from these works provides a broader context for the development of effective compensation and control strategies.

The rest of this paper is organized as follows: Section 2 performs FFT analysis to obtain the harmonic magnitudes and phases. Section 3 incorporates the back-EMF harmonic parameters into the motor model. Section 4 shows the results that were simulated using MATLAB/Simulink R2024a, and experimental results are presented to validate the effectiveness of the back-EMF compensation strategy.

2. Back-EMF Measurement and FFT Analysis Result

2.1. Formulation of the Back-EMF Harmonic Equation

The back-EMF needs to be transformed from the *abc* and *xyz* phases to the dq-axes equations for further analysis. Appendix A shows the Clarke and Park transformation matrices. The six-phase back-EMF equations for the *abc* and *xyz* phases, considering only harmonic components and neglecting the fundamental component, are given as follows:

$$e_{a-h} = -\omega_r \lambda'_m \left[\sum_{n=5,7,11,13} h_{an} \sin(n\theta_a + \delta_{an}) \right]$$

$$e_{b-h} = -\omega_r \lambda'_m \left[\sum_{n=5,7,11,13} h_{an} \sin\left(n\theta_a - n\frac{2}{3}\pi + \delta_{an}\right) \right] \tag{1}$$

$$e_{c-h} = -\omega_r \lambda'_m \left[\sum_{n=5,7,11,13} h_{an} \sin\left(n\theta_a + n\frac{2}{3}\pi + \delta_{an}\right) \right]$$

$$e_{x-h} = -\omega_r \lambda'_m \left[\sum_{n=5,7,11,13} h_{xn} \sin(n\theta_x + \delta_{xn}) \right]$$

$$e_{y-h} = -\omega_r \lambda'_m \left[\sum_{n=5,7,11,13} h_{xn} \sin\left(n\theta_x - n\frac{2}{3}\pi + \delta_{xn}\right) \right] \tag{2}$$

$$e_{z-h} = -\omega_r \lambda'_m \left[\sum_{n=5,7,11,13} h_{xn} \sin\left(n\theta_x + n\frac{2}{3}\pi + \delta_{xn}\right) \right]$$

In this context, $\theta_x = \theta_a - \frac{1}{6}\pi$, h_{an}, and h_{xn} represent the harmonic content of the *a*-phase and *x*-phase, respectively, with n indicating the order of the harmonics. These values reflect the percentage of harmonic components relative to the fundamental wave. δ_{an} and δ_{xn} denote the harmonic phase angles of *a*-phase and *x*-phase in degrees (°). For n, values of 5, 7, 11, and 13 are considered to obtain the six-phase back-EMF.

The 5th, 7th, 11th, and 13th harmonic components, when transformed into the *dq*-axes via Clarke and Park transformations, correspond to the 6th- and 12th-order harmonics. Appendix A Equation (A7) shows the transformation process. These harmonics align with the natural frequency characteristics of a three-phase system. In a six-phase PMSM, which can be modeled as two independent three-phase subsystems with a 120° phase

shift, the presence of 6th-order harmonics can induce interactions between the subsystems, complicating the composite waveform and destabilizing the electromagnetic torque. The 12th-order harmonics, as the second harmonic multiple of the 6th order, exacerbate these issues by interacting with the spatial harmonics of the winding structure, leading to additional torque ripple and increased vibration. Although the *dq*-axes transformation simplifies control by converting three-phase AC currents into DC currents on direct and quadrature axes, the 6th- and 12th-order harmonics introduce coupling effects that compromise the accuracy of decoupling, ultimately degrading control performance.

The compensation strategy for the harmonics in back-EMF along *dq*-axes are as follows:

$$
\begin{aligned}
e_{dqa-h} &= \omega_r \lambda'_m \begin{bmatrix} -h_{d6}\sin(6\theta_a + \delta_{d6}) - h_{d12}\sin(12\theta_a + \delta_{d12}) \\ -h_{q6}\cos(6\theta_a + \delta_{q6}) + h_{q12}\cos(12\theta_a + \delta_{q12}) \end{bmatrix} \\
e_{dqx-h} &= \omega_r \lambda'_m \begin{bmatrix} h_{d6}\sin(6\theta_a + \delta_{d6}) - h_{d12}\sin(12\theta_a + \delta_{d12}) \\ h_{q6}\cos(6\theta_a + \delta_{q6}) + h_{q12}\cos(12\theta_a + \delta_{q12}) \end{bmatrix}
\end{aligned}
\tag{3}
$$

e_{dqa-h} and e_{dqx-h} represent the back-EMF harmonic components for the *abc* and *xyz* phases, respectively. Given that the harmonic components of the six-phase back-EMF exhibit similar characteristics, the harmonics of the sixth and twelfth orders on the dq-axes are denoted as h_{d6}, h_{d12}, h_{q6}, and h_{q12}. Similarly, δ_{d6}, δ_{d12}, δ_{q6}, and δ_{q12} represent the phase angles of the sixth and twelfth-order harmonics on the dq-axes.

2.2. Measurement of Back-EMF

In Figure 1, the operation of the six-phase PMSM is driven by the Dynamometer. The MCU reads the angle and voltage information, which is then transmitted to the PC via USB. LabVIEW processes the data and extracts the harmonic content of the six-phase back-EMF. Figure 2 illustrates the analysis results for 600 rpm, respectively.

During testing, measurements were conducted across a range of speeds from 100 rpm to 1200 rpm. Theoretically, the magnitude of back-EMF is proportional to rotational speed. Consequently, the ratio of harmonic magnitudes to the fundamental back-EMF, as well as their phases, remains consistent across varying speeds. This observation aligns with the experimental results obtained at various speeds. Therefore, 50% of the rated speed was selected to present the findings.
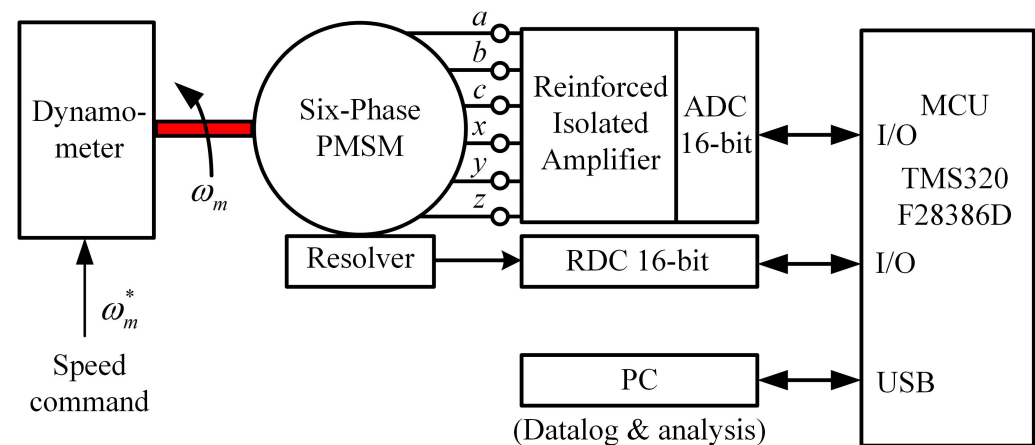
Figure 1. Six-phase PMSM back-EMF measurement system block diagram.
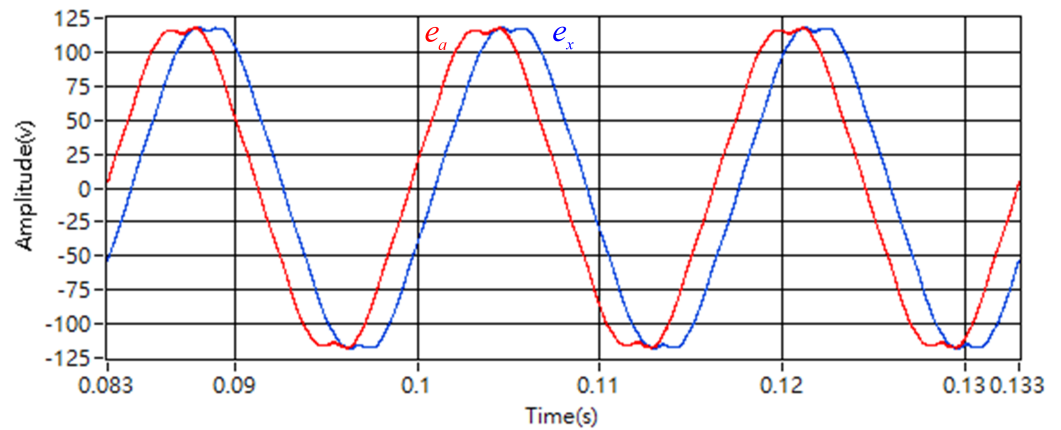
Figure 2. Phase-*a* and phase-*x* back-EMF measurement.

The FFT analysis results from Figure 2 are summarized in Table 1. After simplification using a polar coordinate system, the magnitudes and phases of the 6th and 12th harmonic of dq-axes back-EMF are shown in Table 2. These parameters were used in both the experimental measurements and simulations.

Table 1. Back-EMF harmonic parameters based on phase voltage harmonic distribution.

h_5 (%)/δ_5 (°)	h_7 (%)/δ_7 (°)	h_{11} (%)/δ_{11} (°)	h_{13} (%)/δ_{13} (°)
2.72/185.4	1.58/5.6	0.72/347.9	0.27/173.5

The fundamental peak value of the back-EMF is 118.1 V.

Table 2. Back-EMF harmonic parameters based on dq-axes harmonic distribution.

h_{d6} (%)/δ_{d6} (°)	h_{d12} (%)/δ_{d12} (°)	h_{q6} (%)/δ_{q6} (°)	h_{q12} (%)/δ_{q12} (°)
1.03/5.7	0.48/165.1	3.94/94.7	0.95/260.5

2.3. Back-EMF Reconstruction

To expand upon the current analysis, it is crucial to further discuss the role of harmonic components in the back-EMF reconstruction process. The presence of 6th and 12th harmonics in the dq-axes plays a significant role in influencing the waveform accuracy of back-EMF. These harmonic components are primarily caused by the spatial distribution of stator windings and the magnetic flux within the motor. By analyzing the harmonics in the dq-axes, the method of reconstructing back-EMF can be made more efficient and accurate, which is essential for improving overall system performance in PMSM.

Through Equation (3), we reconstructed the back-EMF and compared it with the measured back-EMF in phases-*a* and phase-*x*. As shown in Figure 3, the results align, confirming the accuracy of the equation. In the next section, we convert this equation into common-mode and differential-mode forms to further simplify the expressions.

In Figure 3b, it can be clearly observed that phase-*x* lags phase-*a* by 0.00139 s. At a speed of 600 rpm and with a motor pole count of 12, the electrical frequency is 60 Hz. Therefore, a lag of 0.00139 s corresponds to an electrical angle of 30 degrees, which verifies that the phase voltage of phase-*x* lags behind that of phase-*a*.

(**a**)

(**b**)
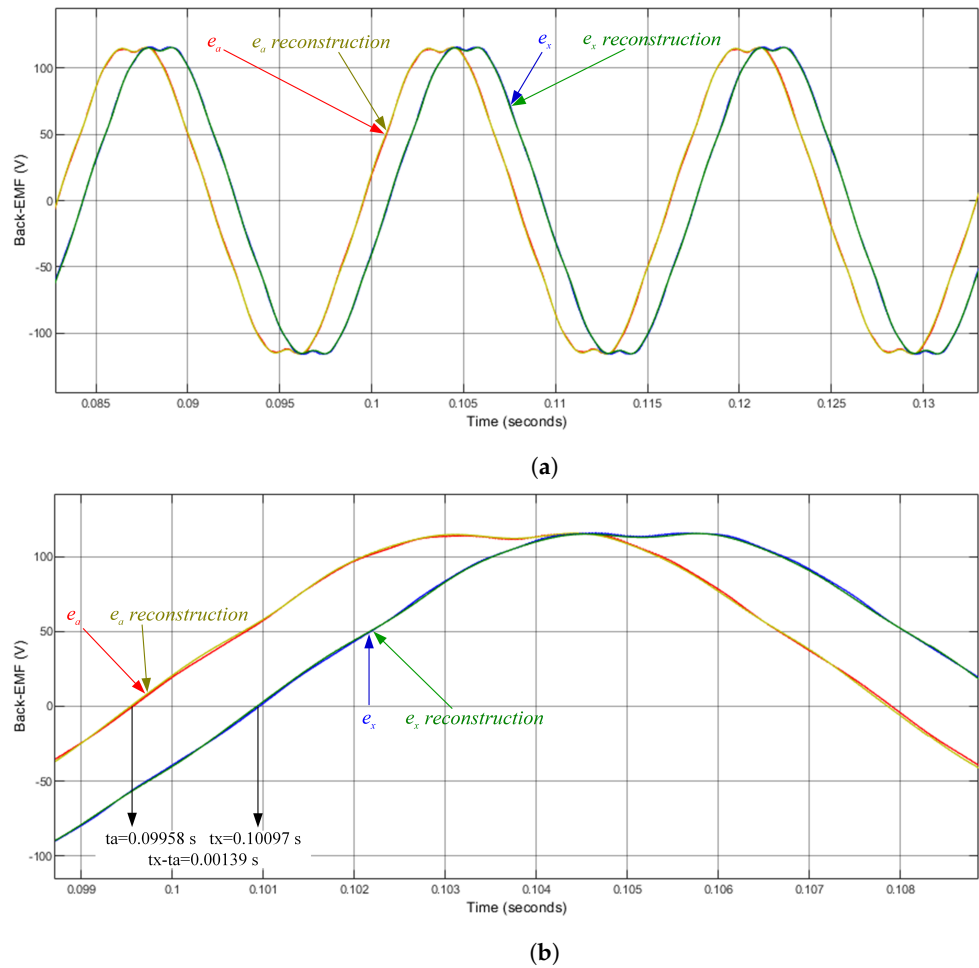
Figure 3. The waveform of the measured and reconstructed phase-*a* and phase-*x* back-EMF: (**a**) phase-*a* and phase-*x* back-EMF waveform; (**b**) zoomed-in waveform.

3. Incorporate the Back-EMF Harmonics into the Six-Phase PMSM Motor Model

When formulating the dq-axes flux linkage equations for the six-phase PMSM while neglecting the zero-sequence current.

$$
\begin{aligned}
\lambda_{da} &= L_d i_{da} + M_d i_{dx} + \lambda'_m \\
\lambda_{dx} &= L_d i_{dx} + M_d i_{da} + \lambda'_m \\
\lambda_{qa} &= L_q i_{qa} + M_q i_{qx} \\
\lambda_{qa} &= L_q i_{qx} + M_q i_{qa}
\end{aligned}
\tag{4}
$$

The dq-axes voltage equations of the six-phase PMSM, incorporating the effects of back-EMF harmonics, are presented below in a simplified form.

$$
\begin{aligned}
v_{da} &= R_s i_{da} + \frac{d}{dt}\lambda_{da} - \omega_r \lambda_{qa} + e_{da-h} \\
v_{qa} &= R_s i_{qa} + \frac{d}{dt}\lambda_{qa} + \omega_r \lambda_{da} + e_{qa-h} \\
v_{dx} &= R_s i_{dx} + \frac{d}{dt}\lambda_{dx} - \omega_r \lambda_{qx} + e_{dx-h} \\
v_{qx} &= R_s i_{qx} + \frac{d}{dt}\lambda_{qx} + \omega_r \lambda_{dx} + e_{qx-h}
\end{aligned}
\tag{5}
$$

The transformation matrix equations for common-mode and differential-mode can be found in Appendix A.

$$\lambda_d^+ = \frac{1}{2}(\lambda_{da} + \lambda_{dx}) = L_d^+ i_d^+ + \lambda_m'$$

$$\lambda_q^+ = \frac{1}{2}(\lambda_{qa} + \lambda_{qx}) = L_q^+ i_q^+$$

$$\lambda_d^- = \frac{1}{2}(\lambda_{da} - \lambda_{dx}) = L_d^- i_d^-$$

$$\lambda_q^- = \frac{1}{2}(\lambda_{qa} - \lambda_{qx}) = L_q^- i_q^-$$

(6)

With the inclusion of the dq-axes voltage equations of the six-phase PMSM considering the back-EMF harmonics, the equations can be transformed into common-mode and differential-mode voltage equations through common-mode and differential-mode transformations.

$$v_d^+ = \frac{1}{2}(v_{da} + v_{dx}) = R_s i_d^+ + \frac{d}{dt}\lambda_d^+ - \omega_r \lambda_q^+ + e_{d-h}^+$$

$$v_q^+ = \frac{1}{2}(v_{qa} + v_{qx}) = R_s i_q^+ + \frac{d}{dt}\lambda_q^+ + \omega_r \lambda_d^+ + e_{q-h}^+$$

$$v_d^- = \frac{1}{2}(v_{da} - v_{dx}) = R_s i_d^- + \frac{d}{dt}\lambda_d^- - \omega_r \lambda_q^- + e_{d-h}^-$$

$$v_q^- = \frac{1}{2}(v_{qa} - v_{qx}) = R_s i_q^- + \frac{d}{dt}\lambda_q^- + \omega_r \lambda_d^- + e_{q-h}^-$$

(7)

The definitions of common-mode and differential-mode inductances are $L_d^+ = L_d + M_d$, $L_q^+ = L_q + M_q$, $L_d^- = L_d - M_d$, $L_q^- = L_q - M_q$. The definitions of common-mode and differential-mode currents are $i_d^+ = \frac{1}{2}(i_{da} + i_{dx})$, $i_q^+ = \frac{1}{2}(i_{qa} + i_{qx})$, $i_d^- = \frac{1}{2}(i_{da} - i_{dx})$, $i_q^- = \frac{1}{2}(i_{qa} - i_{qx})$.

$$e_{d-h}^+ = \frac{1}{2}(e_{da} + e_{dx}) = \omega_r \lambda_m'[-h_{d12}\sin(12\theta_a + \delta_{d12})]$$

$$e_{q-h}^+ = \frac{1}{2}(e_{qa} + e_{qx}) = \omega_r \lambda_m'[h_{q12}\cos(12\theta_a + \delta_{q12})]$$

$$e_{d-h}^- = \frac{1}{2}(e_{da} - e_{dx}) = \omega_r \lambda_m'[-h_{d6}\sin(6\theta_a + \delta_{d6})]$$

$$e_{q-h}^- = \frac{1}{2}(e_{qa} - e_{qx}) = \omega_r \lambda_m'[-h_{q6}\cos(6\theta_a + \delta_{q6})]$$

(8)

After converting the back-EMF harmonics equations to common-mode and differential-mode forms, these parameters are used in feed-forward compensation. Additionally, the back-EMF was reconstructed using this equation, yielding results consistent with those in Section 2. Figure 3 further validates the reliability of this approach. The overall control block diagram is shown in Figure 4.

$$v_d^{+*} = u_d^{+*} - \omega_r \lambda_q^+ + e_{d-h}^+$$

$$v_q^{+*} = u_q^{+*} + \omega_r \lambda_d^+ + e_{q-h}^+$$

$$v_d^{-*} = u_d^{-*} - \omega_r \lambda_q^- + e_{d-h}^-$$

$$v_q^{-*} = u_q^{-*} + \omega_r \lambda_d^- + e_{q-h}^-$$

(9)

$$u_d^{+*} = G_d^+(s) \circ \triangle i_d^+$$

$$u_q^{+*} = G_q^+(s) \circ \triangle i_q^+$$

$$u_d^{-*} = G_d^-(s) \circ \triangle i_d^-$$

$$u_q^{-*} = G_q^-(s) \circ \triangle i_q^-$$

(10)

The current control loops are implemented with a PI controller. The symbol "^" within the diagram represents the measured feedback value, and "*" represents the commands.

The errors between the commands and feedback are represented as $\triangle i_d^+$, $\triangle i_q^+$, $\triangle i_d^-$, and $\triangle i_q^-$. The gains of the current regulators are defined as $G_d^+(s)$, $G_q^+(s)$, $G_d^-(s)$, and $G_q^-(s)$.
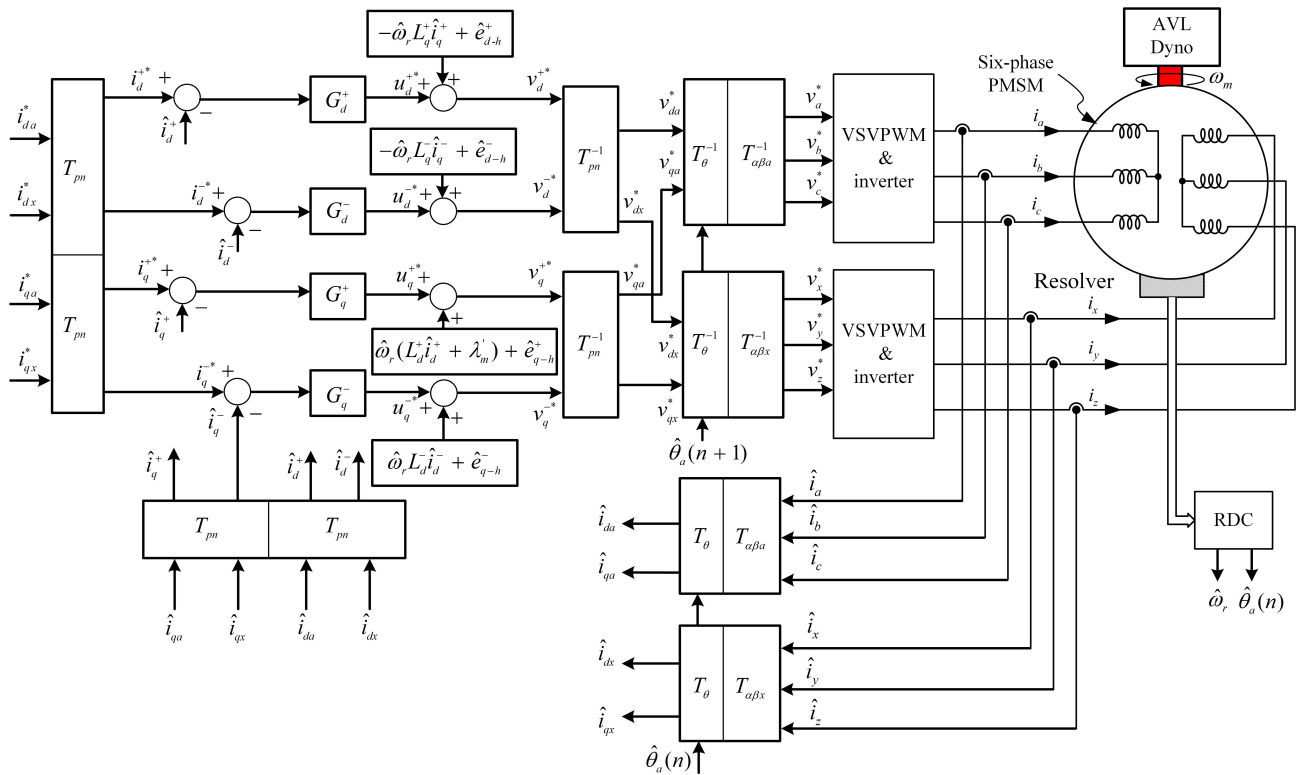
Figure 4. Six-phase PMSM common-mode and differential-mode current closed-loop control block.

4. Result

Appendix A, Table A1 shows that the rated motor speed is 1200 rpm. To evaluate performance across a range of operating conditions, tests were conducted at speeds of 300, 600, 900, and 1200 rpm, corresponding to 25%, 50%, 75%, and 100% of the rated speed. The current THD results from both simulation and experimental measurements at the aforementioned speeds are comprehensively summarized in Table 3.

Table 3. Current harmonic reduction with back-EMF compensation (simulation and actual result).

Speed (rpm)	I_m (A)	THD-No Comp. (%) Simulation/Actual	THD-Comp. (%) Simulation/Actual	Reduction (%) Simulation/Actual
300	100	8.16/9.08	3.64/4.01	55.39/55.84
300	200	3.59/4.91	1.71/2.86	52.37/41.75
600	100	16.33/15.00	7.50/4.11	54.07/72.60
600	200	7.05/8.34	3.55/4.90	49.65/41.25
900	100	21.90/19.99	12.80/5.15	41.55/74.24
900	200	9.93/11.86	6.68/6.83	32.73/42.41
1200	100	25.74/25.31	19.35/7.14	24.83/71.79
1200	200	12.40/15.98	10.32/9.46	16.77/40.80

The inverter operated at a switching frequency of $f_s = 10$ kHz with a dead time of 2 μs, and currents for comparison include $i_{da}^* = i_{dx}^* = -50\sqrt{2}$ A, $i_{qa}^* = i_{qx}^* = 50\sqrt{2}$ A, and $i_{da}^* = i_{dx}^* = -100\sqrt{2}$ A, $i_{qa}^* = i_{qx}^* = 100\sqrt{2}$ A, resulting in the peak phase currents I_m of 100 A and 200 A. With 12 poles, the motor completes one mechanical rotation every six electrical cycles, and results are shown for six steady-state electrical cycles. The waveform for 900 rpm is specifically highlighted in the results, as this speed exhibited the most significant

performance in terms of motor operation and harmonic analysis. This observation was consistent across tests, irrespective of whether the peak phase current was 100 A or 200 A, further reinforcing the importance of this operating point for detailed analysis.

4.1. Simulation Result

Figure 5a shows the simulation results at 900 rpm with a peak phase current I_m of 200 A, without back-EMF harmonic compensation, revealing current waveform distortion. In contrast, Figure 5b shows improved waveform quality with back-EMF harmonic compensation under the same conditions. Figure 6 summarizes and compares the THDs of all scenarios, demonstrating the effectiveness of back-EMF harmonic compensation in reducing current harmonic distortion and enhancing motor drive stability.

(a)

(b)
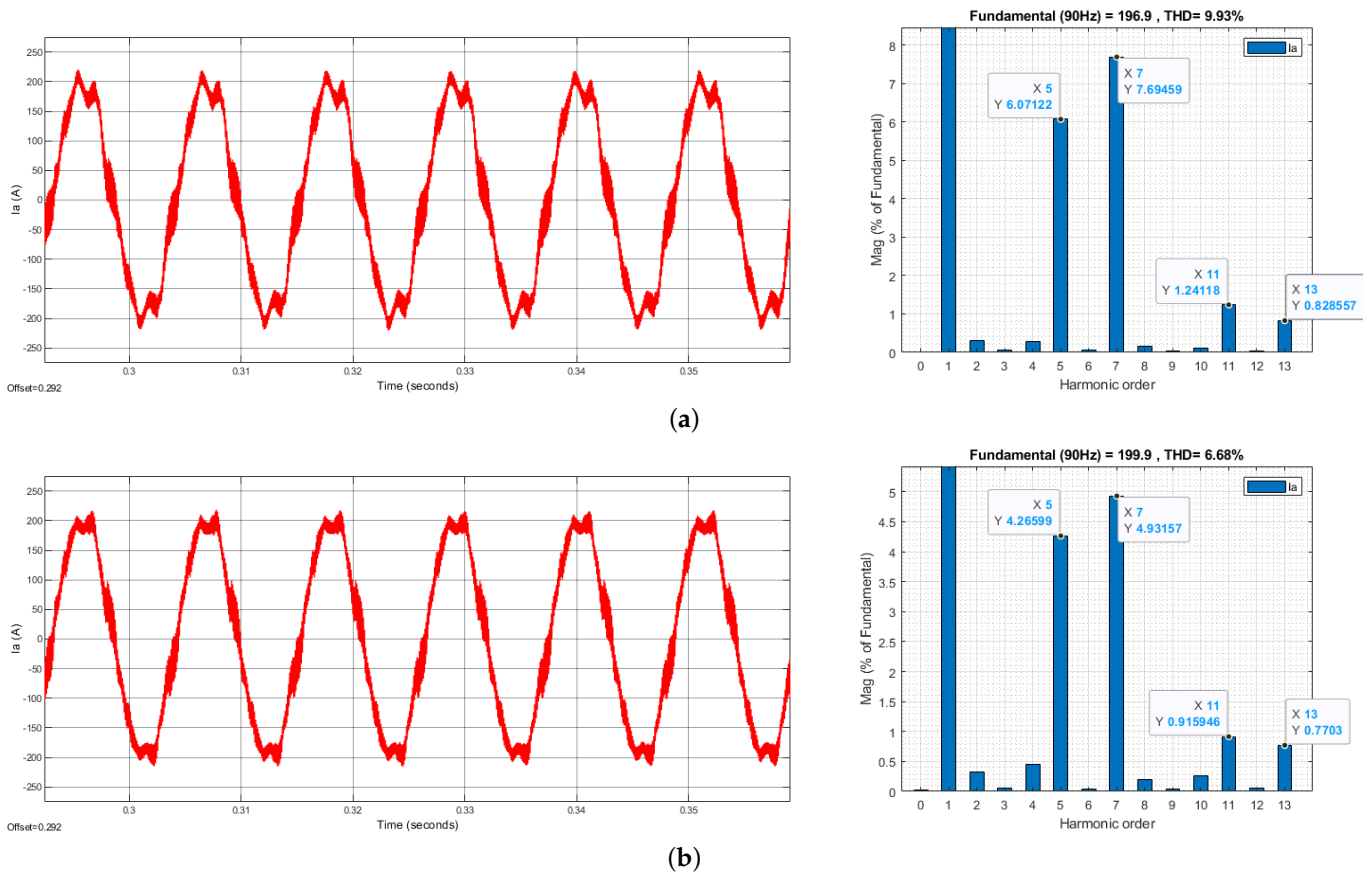
Figure 5. Simulated phase-*a* current waveform and harmonic histogram: (**a**) Without compensation. (**b**) With compensation.
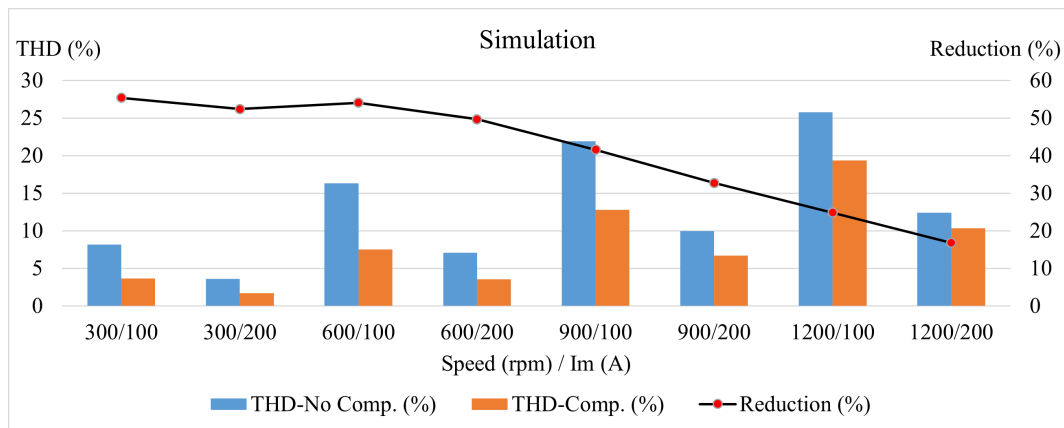
Figure 6. Histogram of the THD reduction in simulation result.

4.2. Actual Result

Figure 7a shows an actual photograph of the experimental setup where the dynamometer drives the six-phase PMSM. Figure 7b presents the housing of the actual drive system, along with the control and feedback circuits. Real-time voltage and current data are sampled at a 10 kHz sampling frequency on the driver and then transmitted to PC. The data are recorded and subsequently processed using MATLAB/Simulink for FFT analysis.

(**a**)
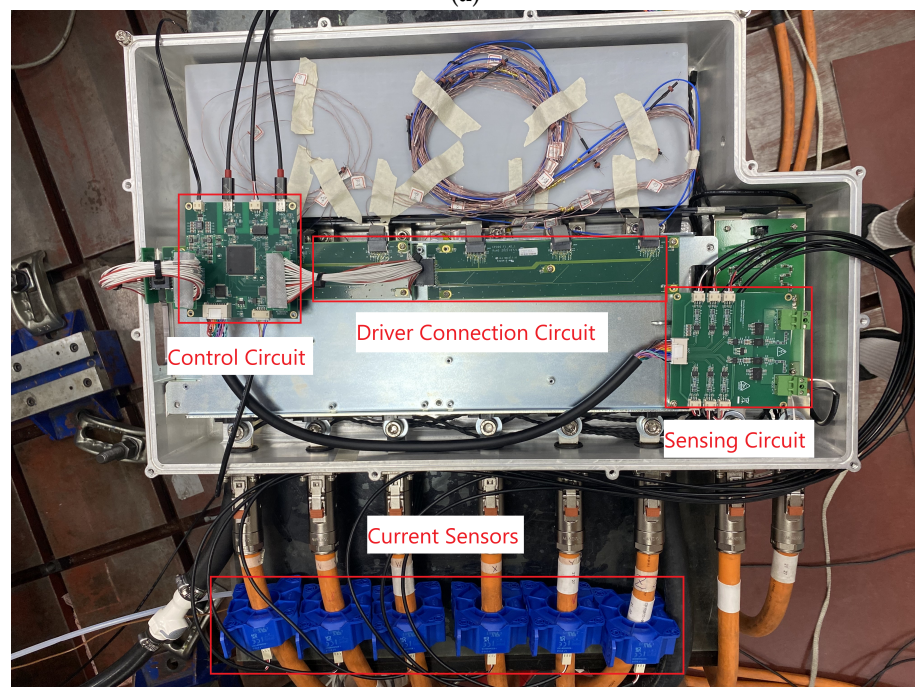
(**b**)

Figure 7. Photos of the six-phase PMSM testbench: (**a**) Setup with the dynamometer driving the six-phase PMSM. (**b**) Six-phase PMSM drive system.

Figure 8a illustrates the actual performance without the incorporation of back-EMF harmonic compensation, demonstrating the effects of harmonics on the system's response. Conversely, Figure 8b presents the performance under identical speed and current commands but with harmonic compensation applied, highlighting the improvement in waveform fidelity. The THD of the current is summarized and compared in Figure 9, providing quantitative evidence of the effectiveness of harmonic compensation in reducing distortions and enhancing system performance. This comparison clearly demonstrates the positive impact of back-EMF harmonic compensation on system stability and control precision.
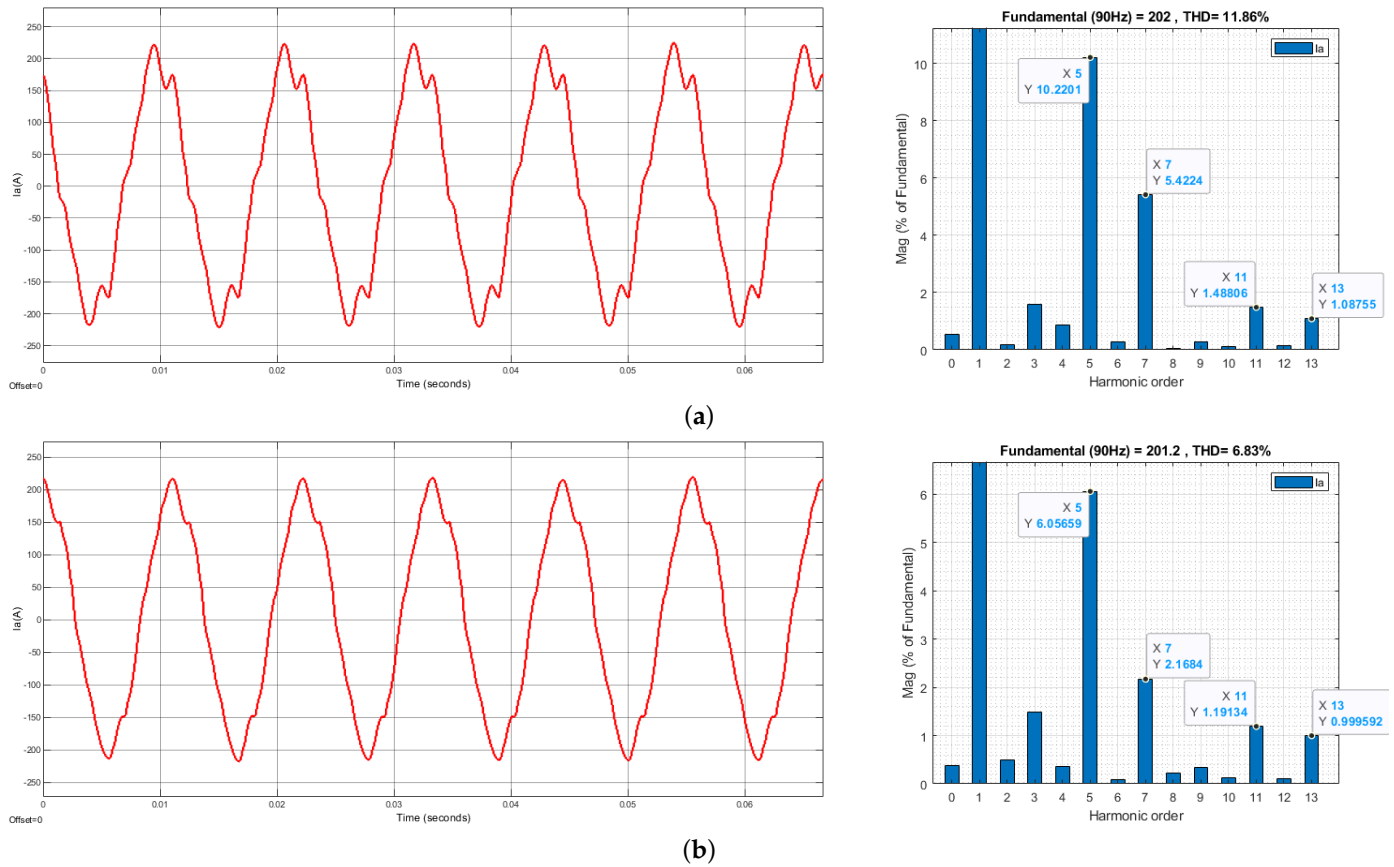
Figure 8. Actual phase-*a* current waveform and harmonic histogram: (**a**) Without compensation. (**b**) With compensation.
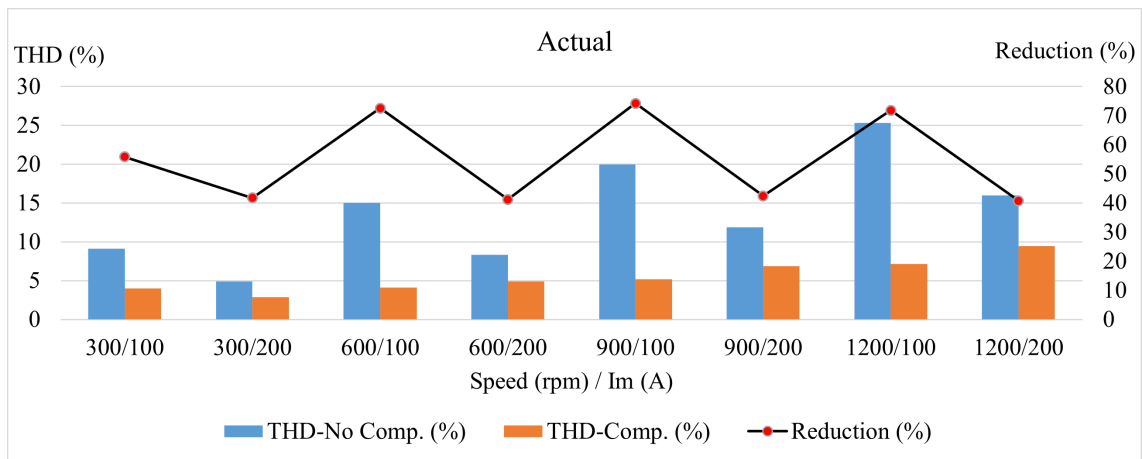
Figure 9. Histogram of the THD reduction in actual result.

5. Discussion

In Section 4, as shown in Figures 6 and 9 , the summarized data indicate that as the rotational speed increases, the current harmonic component in the six-phase PMSM rises as well. The primary reason for this is that the rotor frequency of the PMSM increases with speed, while the switching frequency of the inverter typically remains constant. Consequently, the ratio between the rotor frequency and the inverter's switching frequency decreases, making it more challenging for the inverter to follow the rapidly changing commands effectively. This results in less smooth current waveforms at higher speeds compared with lower speeds, thereby leading to an increase in harmonic content. Therefore, under the same speed and current command conditions, increasing the inverter's switching frequency could reduce the current harmonic content. Additionally, as the rotor frequency rises, higher-order harmonics further exacerbate the challenge for the inverter to track the rapidly varying voltage commands due to the static switching frequency, which may pose certain challenges for this compensation method at higher rotational speeds.

When operating at the same speed but with a lower current, the current waveform shows greater improvement. This is because, at lower currents, the waveform is more susceptible to electromagnetic interference, resulting in higher inherent THD in the current when back-EMF harmonic compensation is not applied. Additionally, when the current is lower, the internal resistance voltage drop and inductive voltage drop are also smaller compared with higher currents, causing the back-EMF generated within the motor to dominate the voltage equation. This explains why back-EMF harmonic compensation results in a more significant improvement in the current waveform under lower current conditions.

The results show that, although the compensation is effective, there is still room for improvement. In addition to the back-EMF harmonic compensation, future work will incorporate other current harmonic suppression strategies to further reduce low-order current harmonics and enhance motor performance.

6. Conclusions

The core focus of this paper is back-EMF harmonic compensation; however, the procedure behind implementing this compensation is crucial. The first step involves the analysis of back-EMF, where not only the harmonic magnitude but, more importantly, the phase of the harmonics must be taken into account. Accurate phase alignment and correct harmonic magnitude are essential to reconstruct the original back-EMF waveform. Once this waveform is obtained, the compensation strategy can be integrated into the controller to realize the back-EMF harmonic compensation.

This study addresses the issue of low-order current harmonic distortions caused by the coupling between two sets of three-phase windings in a six-phase PMSM, a challenge that represents a significant drawback of six-phase motors compared with their three-phase counterparts. However, the method proposed in this paper offers a substantial improvement by effectively mitigating these distortions, thus enhancing the performance and broadening the applicability of six-phase PMSM. The dual three-phase configuration is primarily adopted to provide redundancy, ensuring continuous operation even if one set of windings fails. This feature is particularly advantageous for electric vehicle (EV) applications, where system reliability is critical. By addressing both harmonic distortion and fault-tolerant operation, the proposed approach not only strengthens the robustness of EV systems but also demonstrates its potential for broader applications across various fields requiring high reliability and fault tolerance.

In the experimental results, the THD reduction ratio ranged from 40.80% to 74.24%. The THD with back-EMF harmonic compensation was significantly lower compared with that without compensation. These results clearly demonstrate that this compensation strategy effectively enhances the performance of the six-phase PMSM.

Author Contributions: Conceptualization, J.-C.H. and P.-S.H.; methodology, J.-C.H. and Y.-T.L.; software, P.-S.H.; validation, J.-C.H., P.-S.H. and C.-T.T.; formal analysis, P.-S.H. and C.-T.T.; investigation, P.-S.H. and C.-T.T.; resources, J.-C.H., C.-T.L., and Y.-T.L.; data curation, P.-S.H. and C.-T.T.; writing—original draft preparation, C.-T.T.; writing—review and editing, J.-C.H. and P.-S.H.; visualization, J.-C.H., P.-S.H., and C.-T.T.; supervision, J.-C.H.; project administration, J.-C.H. and C.-T.L.; funding acquisition, J.-C.H. All authors have read and agreed to the published version of the manuscript.

Abbreviations

The following abbreviations are used in this manuscript:

Back-EMF	Back-Electromotive Force
THD	Total Harmonic Distortion
PMSM	Permanent-Magnet Synchronous Motor
FOC	Field-Oriented Control
FFT	Fast Fourier Transform
comp.	Compensation

Appendix A

Table A1. Motor Specifications.

Parameter	Value
DC link voltage (V)	600
Rated Speed (rpm)	1200
Poles N_p	12
Phase resistance R_s (mΩ)	23.14
d-axis self inductance L_d (μH)	309.9
q-axis self inductance L_q (μH)	743.2
d-axis mutual inductance M_d (μH)	260.3
q-axis mutual inductance M_q (μH)	706.1
Flux linkage λ'_m (Wb)	0.313

$$T_{\alpha\beta a} = \frac{2}{3}\begin{bmatrix} 1 & -\frac{1}{2} & -\frac{1}{2} \\ 0 & \frac{\sqrt{3}}{2} & -\frac{\sqrt{3}}{2} \end{bmatrix}, T_{\alpha\beta a}^{-1} = \begin{bmatrix} 1 & 0 \\ -\frac{1}{2} & \frac{\sqrt{3}}{2} \\ -\frac{1}{2} & -\frac{\sqrt{3}}{2} \end{bmatrix} \tag{A1}$$

$$T_{\alpha\beta x} = \frac{2}{3}\begin{bmatrix} \frac{\sqrt{3}}{2} & -\frac{\sqrt{3}}{2} & 0 \\ \frac{1}{2} & \frac{1}{2} & -1 \end{bmatrix}, T_{\alpha\beta x}^{-1} = \begin{bmatrix} \frac{\sqrt{3}}{2} & \frac{1}{2} \\ -\frac{\sqrt{3}}{2} & \frac{1}{2} \\ 0 & -1 \end{bmatrix} \tag{A2}$$

$$T_\theta = \begin{bmatrix} \cos\theta_a & \sin\theta_a \\ -\sin\theta_a & \cos\theta_a \end{bmatrix}, T_\theta^{-1} = \begin{bmatrix} \cos\theta_a & -\sin\theta_a \\ \sin\theta_a & \cos\theta_a \end{bmatrix} \tag{A3}$$

$$T_{dqa} = T_\theta T_{\alpha\beta a} = \frac{2}{3}\begin{bmatrix} \cos\theta_a & \cos(\theta_a - \frac{2}{3}\pi) & \cos(\theta_a + \frac{2}{3}\pi) \\ -\sin\theta_a & -\sin(\theta_a - \frac{2}{3}\pi) & -\sin(\theta_a + \frac{2}{3}\pi) \end{bmatrix}$$

$$T_{dqa}^{-1} = T_{\alpha\beta a}^{-1} T_\theta^{-1} = \begin{bmatrix} \cos\theta_a & -\sin\theta_a \\ \cos(\theta_a - \frac{2}{3}\pi) & -\sin(\theta_a - \frac{2}{3}\pi) \\ \cos(\theta_a + \frac{2}{3}\pi) & -\sin(\theta_a - \frac{2}{3}\pi) \end{bmatrix} \tag{A4}$$

$$T_{dqx} = T_\theta T_{\alpha\beta x} = \frac{2}{3}\begin{bmatrix} -\sin(\theta_a - \frac{2}{3}\pi) & -\sin(\theta_a + \frac{2}{3}\pi) & -\sin\theta_a \\ -\cos(\theta_a - \frac{2}{3}\pi) & -\cos(\theta_a + \frac{2}{3}\pi) & -\cos\theta_a \end{bmatrix}$$

$$T_{dqx}^{-1} = T_{\alpha\beta x}^{-1} T_\theta^{-1} = \begin{bmatrix} -\sin(\theta_a - \frac{2}{3}\pi) & -\cos(\theta_a - \frac{2}{3}\pi) \\ -\sin(\theta_a + \frac{2}{3}\pi) & -\cos(\theta_a + \frac{2}{3}\pi) \\ -\sin\theta_a & -\cos\theta_a \end{bmatrix} \tag{A5}$$

$$T_{pn} = \frac{1}{2}\begin{bmatrix} 1 & 1 \\ 1 & -1 \end{bmatrix}, T_{pn}^{-1} = \begin{bmatrix} 1 & 1 \\ 1 & -1 \end{bmatrix} \tag{A6}$$

$$e_{dqa-h} = T_{dqa}e_{abc-h}$$
$$e_{dqx-h} = T_{dqx}e_{xyz-h} \tag{A7}$$

References

1. Jiao, N.; Li, Z.; Mao, S.; Sun, C.; Liu, W. Aircraft Brushless Wound-Rotor Synchronous Starter–Generator: A Technology Review. *IEEE Trans. Power Electron.* **2023**, *38*, 7558–7574. [CrossRef]
2. Buticchi, G.; Wheeler, P.; Boroyevich, D. The More-Electric Aircraft and Beyond. *Proc. IEEE* **2023**, *111*, 356–370. [CrossRef]
3. Liu, S.; Liu, Y.; Zhang, B.; Liu, C. Full-Speed Region Predictive Current Control Method of Symmetrical Series-Winding PMSM with Higher DC-Link Utilization. *IEEE Trans. Ind. Electron.* **2023**, *71*, 5541–5552. [CrossRef]
4. Niu, G.; Liu, S. Demagnetization monitoring and life extending control for permanent magnet-driven traction systems. *Mech. Syst. Signal Process.* **2018**, *103*, 264–279. [CrossRef]
5. Reusser, C.A.; Young, H.A.; Perez Osses, J.R.; Perez, M.A.; Simmonds, O.J. Power Electronics and Drives: Applications to Modern Ship Propulsion Systems. *IEEE Ind. Electron. Mag.* **2020**, *14*, 106–122. [CrossRef]
6. Cha, J.; Yoon, J.; Bong, U.; Hahn, S. A Design Study on HTS Halbach Array for Field Coil of 40 MW Ship Propulsion Motor. *IEEE Trans. Appl. Supercond.* **2023**, *33*, 1–5. [CrossRef]
7. Liu, S.; Song, Z.; Dong, Z.; Liu, Y.; Liu, C. Generic Carrier-Based PWM Solution for Series-End Winding PMSM Traction System With Adaptive Overmodulation Scheme. *IEEE Trans. Transp. Electrif.* **2023**, *9*, 712–726. [CrossRef]
8. Liu, C.; Chau, K.T.; Lee, C.H.T.; Song, Z. A Critical Review of Advanced Electric Machines and Control Strategies for Electric Vehicles. *Proc. IEEE* **2021**, *109*, 1004–1028. [CrossRef]
9. Zhu, Z.Q.; Howe, D. Electrical Machines and Drives for Electric, Hybrid, and Fuel Cell Vehicles. *Proc. IEEE* **2007**, *95*, 746–765. [CrossRef]
10. Yuan, L.; Wei, K.Y.; Hu, B.X.; Chen, S. Current control method with enhanced PI controller for six-phase PM synchronous motor drive. In Proceedings of the 2016 19th International Conference on Electrical Machines and Systems (ICEMS), Chiba, Japan, 13–16 November 2016; pp. 1–6.
11. Levi, E. Multiphase Electric Machines for Variable-Speed Applications. *IEEE Trans. Ind. Electron.* **2008**, *55*, 1893–1909. [CrossRef]
12. Song, Z.; Jia, Y.; Liu, C. Open-Phase Fault-Tolerant Control Strategy for Dual Three-Phase Permanent Magnet Synchronous Machines Without Controller Reconfiguration and Fault Detection. *IEEE Trans. Power Electron.* **2023**, *38*, 789–802. [CrossRef]
13. Furmanik, M.; Vidlák, M.; Rafajdus, P. Current Harmonics Control in Six-Phase PMSM. In Proceedings of the 2022 ELEKTRO, Krakow, Poland, 23–26 May 2022; pp. 1–5.
14. Zhang, X.; Xie, X.; Yao, R. Field oriented control for permanent magnet synchronous motor based on DSP experimental platform.In Proceedings of the 27th Chinese Control and Decision Conference (CCDC), Qingdao, China, 23–25 May 2015; pp. 1870–1875.
15. Zossak, S.; Varecha, P.; Makys, P. Comparison of Field Oriented and Six-step Control for High-speed PMSM Drive. In Proceedings of the 2020 ELEKTRO, Taormina, Italy, 25–28 May 2020; pp. 1–5.
16. Das, P.P.; Satpathy, S.; Bhattacharya, S.; Veliadis, V. A Feedforward-Based Harmonic Current Minimization Method for Six-Phase Permanent Magnet Synchronous Machine Drives. In Proceedings of the 2023 IEEE Energy Conversion Congress and Exposition (ECCE), Nashville, TN, USA, 29 October–2 November 2023; pp. 5290–5296.

17.	Kim, H.; Han, Y.; Lee, K.; Bhattacharya, S. A Sinusoidal Current Control Strategy Based on Harmonic Voltage Injection for Harmonic Loss Reduction of PMSMs With Non-Sinusoidal Back-EMF. *IEEE Trans. Ind. Appl.* **2020**, *56*, 7032–7043. [CrossRef]

18.	Said, N.A.M.; Priestley, M.; Dutta, R.; Fletcher, J.E. Torque ripple minimization in dual inverter open-end winding PMSM drives with non-sinusoidal back-EMFs by harmonic current suppression. In Proceedings of the IECON 2016—42nd Annual Conference of the IEEE Industrial Electronics Society, Florence, Italy, 23–26 October 2016; pp. 2975–2980.

19.	Zhu, H.; Xiao, X.; Li, Y. Permanent magnet synchronous motor current ripple reduction with harmonic back-EMF compensation. In Proceedings of the 2010 International Conference on Electrical Machines and Systems, Incheon, Republic of Korea, 10–13 October 2010; pp. 1094–1097.

20.	Kao, W.T.; Hwang, J.C.; Liu, J.E. Development of Three-Phase Permanent-Magnet Synchronous Motor Drive with Strategy to Suppress Harmonic Current. *Energies* **2021**, *14*, 1583. [CrossRef]

21.	Peng, Z.; Sizov, G.Y.; Demerdash, N.A.O. Comparison of torque ripple minimization control techniques in Surface-Mounted Permanent Magnet Synchronous Machines. In Proceedings of the 2011 IEEE International Electric Machines & Drives Conference (IEMDC), Niagara Falls, ON, Canada, 15–18 May 2011; pp. 188–193.

22.	Zhong, Z.; Li, C.; Yin, X. Current Harmonic Elimination for Dual Three-phase PMSM Based on Flux Linkage Harmonic Closed-loop Control. In Proceedings of the 2021 IEEE 16th Conference on Industrial Electronics and Applications (ICIEA), Chengdu, China, 1–4 August 2021; pp. 672–677.

23.	Zhang, H.; Zhai, X.; Zhang, J.; Bai, X.; Li, Z. Mechanism Analysis of the Effect of the Equivalent Proportional Coefficient of Inertia Control for a Doubly Fed Wind Generator on Frequency Stability in Extreme Environments. *Sustainability* **2024**, *16*, 4965. [CrossRef]

24.	Chen, L.; Chen, M.; Li, B.; Sun, X.; Jiang, F. Optimized Fault Tolerant Control of Dual Three-Phase PMSM Under Open-Switch Faults. *Energies* **2024**, *17*, 5198. [CrossRef]

25.	Zhou, C.; Zhong, R.; Sun, G.; Zhao, D.; Zhao, X.; Jing, G. Fault-Tolerant Direct Torque Control of Five-Phase Permanent Magnet Synchronous Motor under Single Open-Phase Fault Based on Virtual Vectors. *Energies* **2024**, *17*, 2660. [CrossRef]

26.	Lee, Y.-S.; Choo, K.-M.; Lee, C.-H.; An, C.-G.; Yi, J.; Won, C.-Y. Common-Mode Voltage Reduction Method Based on Variable Sampling Frequency Finite Control Set-Model Predictive Control for PMSM Drive Systems. *Energies* **2024**, *17*, 1443. [CrossRef]

27.	Su, R.; Wang, Y.; Deng, H.; Liu, X.; Guan, Y. A Power-RPM Reduced-Order Model and Power Control Strategy of the Dual Three-Phase Permanent Magnet Synchronous Motor in a V/f Framework for Oscillation Suppression. *Energies* **2024**, *17*, 4563. [CrossRef]